ACS OMEGA

Open Access

http://pubs.acs.org/journal/acsodf

Article

Fluorescent Nanoporous Materials from Polypropylene-Based Covalent Adaptable Networks

Radek Coufal,* Kinga Adach, Jiří Zedník, Olga Buchar Klinovská, Stanislav Petrík, and Mateusz Fijalkowski

Cite This: *ACS Omega* 2025, 10, 13954−13965

Read Online

ACCESS | Metrics & More | Article Recommendations | Supporting Information

ABSTRACT: Fluorescent polypropylene-based aerogels from thermoreversibly crosslinked networks have been developed. This facile and efficient synthesis results in low-cost, recyclable, chemically resistant, and highly porous functional materials. This process includes the chemical crosslinking of polypropylene, followed by thermal phase separation and freeze-drying, yielding aerogels with specific surface areas up to 200 m^2/g, according to nitrogen absorption−desorption measurements. This is significantly higher than that previously reported for polypropylene porous materials. Besides characterizations of polymer networks by infrared spectroscopy and differential scanning calorimetry, a suite of analytical techniques was utilized to characterize the skeletal framework of aerogels, including scanning electron microscopy and small-angle X-ray scattering. These methods revealed the highly porous nanostructural features of interconnected 3D networks. The modulation of the excited-state properties of the incorporated luminophore is demonstrated and provides insights into their potential applications. Importantly, the aerogels have a pronounced ability to retain toluene, affecting their fluorescence behavior over an extended time scale. This conceptual study presents a low-cost solution for the preparation of highly porous materials that might offer versatility in functionality and may open the door to further exploration and design of high-performance materials that can act very effectively in the sensing and adsorption of organic molecules. The results also provide an intriguing direction for future research focusing on the molecular mechanisms driving the observed fluorescence modulations.

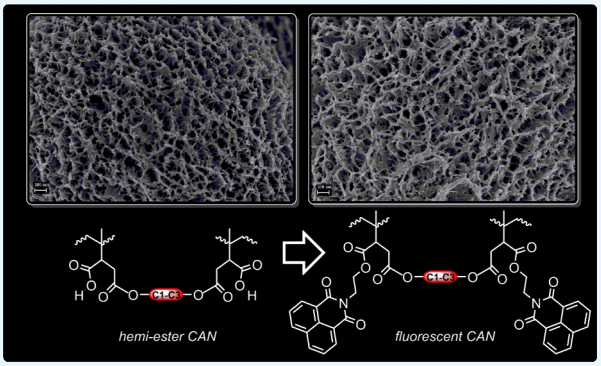

1. INTRODUCTION

Aerogels are an exceptional group of porous materials characterized by their unique properties, such as extremely low density, high surface area, or low thermal conductivity. These materials exhibit a three-dimensional micro/mesoporous structure.[1,2] Aerogels have garnered significant attention in various scientific fields, including catalysis,[3] chemical sensing,[4] energy storage devices,[5] and medical applications.[6] Aerogels can be prepared from their respective gels through several methods, with supercritical fluid drying being the most common. Alternatively, a facile freeze-drying one-step process, which avoids the use of complicated techniques, holds technological significance. Traditional silica aerogels, invented by Kistler[7] in the early 1930s, were surpassed by the emergence of polymer aerogels in 1989.[8] Also, several studies have been devoted to the modification of the silica aerogels with an organic component to resolve the issues with sensitivity to moisture and fragility by endowing hydrophobicity to the system.[9]

Apart from the intrinsic properties of aerogels, polymer aerogels offer improved mechanical properties, flexibility in chemical functionalities, and ease of processing. Currently, aerogels based on polyimide[10−15] and polyurethane[16−19] are the most notable in the literature. However, these materials are often prepared from costly precursors, and their polymer networks typically feature complex backbone structures. Based on the chemical structure, including several functional and aromatic groups, these aerogels may suffer from instability in harsh environments. Moreover, the porous morphology, which is often not easy to fabricate, needs complicated and multistep processes to be prepared. Surprisingly, reports on the fabrication of porous materials based on low-cost, highly resistant, and nonpolar polypropylene (PP) are relatively rare. PP is chemically resistant to solvents, bases, and acids, is a commercially available polymer, is reusable, and is reasonably economical. Especially with regard to the three-dimensional (3D) porous architecture, it is the ideal material for sorption

Received: November 8, 2024
Revised: March 18, 2025
Accepted: March 20, 2025
Published: April 1, 2025

and separation applications. A hydrophobic−superhydrophobic surface allows oil to be attracted very efficiently. In this respect, PP is among the best precursors for preparing super oil sorbents. For instance, Erbil et al.[20] reported a superhydrophobic PP gel-like porous coating. Lin et al.[21] and Othman et al.[22] developed PP macroporous membranes with potential applications in separation processes. Lang et al.[23] and Hong et al.[24] demonstrated excellent separation performance and lipophilic organic loading properties in PP-based composite porous materials. In the similar vein, PP sponges reported by Wang and Uyama[25] and Saleem et al.[26] were proven to be effective sorption materials in practical applications. Furthermore, PP/silica composite aerogel materials reported by Choi et al.[27] and Yoda et al.[28] exhibited enhanced mechanical robustness and low thermal conductivities. However, these materials typically showed specific surface area values well below 100 m^2/g. PP aerogels were also demonstrated to be very potent platforms for the construction of phase-change materials[24,29]

The potential functionalization of the PP chain and subsequent crosslinking could result in a polymer network that serves as a precursor for aerogel fabrication with enhanced structural stability. It has been shown that crosslinked PP provides improved mechanical properties.[30,31] Recently, we demonstrated that crosslinked PP structures could serve as suitable precursors in aerogel processing.[32] By substituting permanent crosslinks with dynamic crosslinking structures, materials can achieve enhanced properties inherent to covalent adaptable networks (CANs).[33] CANs are defined as crosslinked network structures formed by dissociative or associative dynamic covalent bonds between polymer chains, depending on external stimuli.[34,35] The implementation of dynamic bonds presents an interesting approach for directly converting conventionally covalently crosslinked polymers into CANs, offering properties beneficial for material processing, such as reshaping, recycling, or repairing. This attractive chemical strategy, which introduces exchangeable chemical bonds, is a rapidly emerging field, extending the realm of adaptable organic polymer networks.

Functionalizing the nonreactive PP backbone can be challenging. Accordingly, maleic-anhydride-grafted PP may serve as a valuable springboard for constructing CANs based on esterification. This approach offers the additional advantage of retaining reactive carboxyl groups after the hydroxyl groups react with maleic anhydride, forming a hemiester network. Herein, we present the synthesis of PP-based networks with thermoreversible covalent crosslinking and their processing into aerogel materials with high surface areas. Furthermore, as little attention has been paid to the preparation of functionalized aerogels, we introduce 1,8-naphthalimide (NI) units into aerogels by covalent bonding with the polymer network, demonstrating the concept of functional aerogel materials. The NI scaffold and its derivatives play a key role in fluorescent materials and dyes and have found applications in various scientific fields.[36] The aerogel functionalized in this manner would be of considerable research interest, as the conventional sources of fluorescence used in aerogels are heavy-metal-based quantum dots, which raise safety concerns.[37] Additionally, fluorescent polyolefins have attracted significant attention due to their wide range of potential applications in sensing, fluorescent probes, light-emitting diodes, information storage devices, sorting of plastics, quantifying plastic recycling, and more.[38]

To the best of our knowledge, no report on aerogels based on fluorescent adaptable PP networks has been published to date.

2. EXPERIMENTAL SECTION

2.1. Materials. Isotactic polypropylenes grafted with 3 wt % maleic anhydride (iPP-*g*-MA) (P1, commercialized as G3015, Eastman) and with 8−10 wt % maleic anhydride (P2, Sigma-Aldrich), crosslinkers (poly(ethylene glycol)-*block*-poly(propylene glycol)-*block*-poly(ethylene glycol) (M_n = 1100, C1), poly(ethylene glycol)-*block*-poly(propylene glycol)-*block*-poly(ethylene glycol) (M_n = 1900, C2), and glycerol ethoxylate (M_n = 1000, C3) (Sigma-Aldrich)), *N*-(2-hydroxyethyl)-1,8-naphtalimide (NI, 1ClickChemistry Inc.), *N*,*N*-diisopropylethylamine (Sigma-Aldrich), 4-dimethylaminopyridine (DMAP, Sigma-Aldrich), and benzoic anhydride (Sigma-Aldrich) were used as received. Solvents for synthesis and workup obtained from commercial suppliers were used without any further purification.

2.2. Characterization. IR spectra were recorded on an FTIR spectrometer Nicolet iZ10 (Thermo Scientific, USA) with a DTGS detector using the ATR technique, with a spectral resolution of 4 cm^{-1} and a spectral range of 4000−400 cm^{-1}. Variable-temperature IR spectra were recorded on an FTIR spectrometer Nicolet 6700 with MCT/A cryodetector, with a resolution of 2 cm^{-1} and an accumulation of 128 scans (recording of one spectrum took 2 min; temperature corresponds to values at the middle of the measurement period). Spectra were recorded using the DRIFT technique in an in situ chamber under a flow of nitrogen (4.0) with a flow rate of 10 mL/min, heated from 25 °C to the target temperature with a ramp rate of 5 °C/min. The background was measured at 25 °C in the cell with an optical mirror under the flow of nitrogen. The parent polymer P2, supplied as granules, was ground using a CryoMill (Retsch, Germany) before measurement. The grinding process was performed under continuous cooling with liquid nitrogen for 4 min at a frequency of 30 Hz and using zirconium oxide grinding balls and jar. The porosity and total specific surface area were measured by the N_2 adsorption method at the boiling temperature of liquid nitrogen (77 K). Prior to adsorption experiments, samples were evacuated at 40 °C for 12 h. The total surface area was evaluated by using the Brunauer−Emmett−Teller (BET) method. The porosity distribution and average width of pores were evaluated by the Barrett−Joyner−Halenda (BJH) and density functional theory (DFT) methods using the N_2-DFT model with a regularization of 0.1. The experiments were performed with the 3Flex instrument (Micromeritics, Norcross, GA, USA), and the measured parameters were evaluated using Flex software (Micrometrics, Version 6.01). The structural analysis of samples was performed using UHR-FE-SEM Zeiss Ultra Plus. The samples were fixed on aluminum stubs using double-sided carbon tape; the samples were not modified or metal-coated before the analysis. Gentle beam conditions, including a low accelerating voltage of 1 kV and low probe currents >1 pA, were used to obtain images because of the beam sensitivity and low average atomic number of the observed material. The images in topographical contrast were acquired using a highly efficient InLens secondary electron detector. The fluorescence spectra of the powder samples were measured in the solid state. Samples were prepared on microscope ground glass slides, which were precoated with a thin layer of carbon in a vacuum

https://doi.org/10.1021/acsomega.4c10168
ACS Omega 2025, 10, 13954−13965

deposition chamber. The luminophore-polymer samples were then mounted on the carbon-coated slides using an Entellan microscopic adhesive. A small drop of adhesive was placed on the slide, and the solid sample was carefully deposited into the adhesive using a spatula. Once the samples were applied, they were cured on a heating plate set to 60 °C for 15 min to ensure proper adhesion and adhesive hardening. After curing, any excess sample material was removed using compressed air to clean the surface. Excitation and emission spectra were recorded using a Horiba Jobin Yvon Spex 3 spectrofluorometer. All spectra were corrected using the factory calibration functions to ensure accuracy. Emission spectra were excited at 370 nm and measured at a detection angle of 22.5° relative to the excitation beam. For time-resolved fluorescence measurements, decay profiles were acquired using a laser diode (372 nm), with the decay signals recorded using the single-photon counting technique. The experimental setup was blank-controlled, with comparison spectra collected to account for background noise and to ensure reliable data interpretation. In the time-resolved fluorescence decay experiments, the excitation diode was held constant at 372 nm, while the emission decay was measured at different wavelengths across the 395−500 nm range, with a step size of 5 nm. The steady-state spectra and time-resolved measurements were combined, and a detailed analysis of the time-resolved emission spectra (TRES) was performed. This approach allowed for the observation of emission dynamics at multiple wavelengths, providing comprehensive insights into the decay behavior of the luminophore within the polymer matrix. Differential scanning calorimetry (DSC) was performed to evaluate the thermal properties. A differential scanning calorimeter (a Metller Toledo DSC1 Star unit) was employed for thermal analysis to discern the differences in heat between the PP networks. The samples were heated from 25 to 190 °C in an inert nitrogen atmosphere at a flow rate of 50 mL/min. Thermal gravimetric analysis (TGA) was carried out using a TGA Q500 instrument to investigate the thermal stability of the aerogels. Small-angle X-ray scattering (SAXS) studies were performed on SAXSPoint 2.0 instrument (Anton Paar) with a MetalJet X-ray source (Excillum) with 1.34 Å wavelength and an Eiger R 1 M Horizontal detector at a sample detector distance of 777 mm, using beamstop (2 mm Si) and 30s acquisition time for each frame (10). Data analysis was conducted with the SASfit[39] tool for modeling and analysis of small-angle scattering.

2.3. Typical Procedure for the Synthesis of Cross-linked PP Materials. iPP-*g*-MA, **P1** (6 g), was dissolved in *p*-xylene (100 mL) at 120 °C (30−60 min). Then, *N*,*N*-diisopropylethylamine (0.9 mL), 4-dimethylaminopyridine (19 mg), and benzoic anhydride (0.42 g) were added, and the resulting mixture was stirred for 10 min. Next, the crosslinker **C1** (in an equimolar ratio of OH/maleic anhydride) dissolved in *p*-xylene (10 mL) was slowly added, and the resulting stirred mixture was allowed to react at 120 °C overnight. After cooling to room temperature, acetone (50 mL) was added, the mixture was filtered on sintered glass, and the solid was rinsed with ethanol (2 × 50 mL) and acetone (2 × 50 mL). The product was dried in vacuo (10 mbar, at least 2 h). This procedure formed a white−off-white powder in an isolated yield of 5.5−6 g.

2.4. Typical Procedure for the Functionalization of PP Networks with 1,8-Naphthalimide (NI). P1C1 (3 g) was dissolved in *p*-xylene (50 mL) at 120 °C (30−60 min). Then, *N*,*N*-diisopropylethylamine (0.5 mL), 4-dimethylaminopyridine (23 mg), and benzoic anhydride (0.20 g) were added, and the resulting mixture was stirred for 10 min. Next, *N*-(2-hydroxyethyl)-1,8-naphtalimide (178 mg) was slowly added, and the resulting stirred mixture was allowed to react at 120 °C overnight. After cooling to room temperature, acetone (50 mL) was added, the mixture was filtered on sintered glass, and the solid was rinsed with chloroform (2 × 50 mL), ethanol (2 × 50 mL), and acetone (2 × 50 mL). The product was dried in vacuo (10 mbar, at least 2 h). This procedure formed a white−off-white powder in an isolated yield of 2.8−2.9 g.

Assignment of **PXCY** refers to polymer/aerogel produced from polymer **PX** (X = 1, 2) and crosslinker **CY** (Y = 1, 2, 3). **PXCYF** refers to polymer/aerogel functionalized with a fluorescent **NI** unit.

2.5. Typical Gelation and Drying Procedure. The powdered samples were dissolved in *p*-xylene (typically 100 mg/mL) at 120 °C (30−60 min). Thereafter, the systems were quenched to a desired temperature to solidify and poured into cellulose tubes saturated with xylene (airtight plastic tubes). The gels, which formed within 30 min, were aged in the molds. The solvent within the gels was then gradually exchanged with acetone in 24 h intervals starting with 25% *p*-xylene in acetone, followed by pure acetone (6×). Thereafter, the home-built freeze-drying (liquid N_2, 0.3 mbar) apparatus was used to obtain aerogels from the respective gels (Figure S1). The device consisted of a rotary oil pump, which was connected to the cold trap via a separation valve that protected the pump against oil contamination. At the end of the system, there was a stainless steel vacuum chamber (75 mL) with an additional vacuum port enabling vacuum level measurement. Additionally, a needle valve was used to slowly aerate the system after the solvent extraction process. The samples were placed in a chamber filled with liquid nitrogen, and then the entire chamber was immersed in liquid nitrogen to completely cool down. In the next step, the system was evacuated to 0.3 mbar and kept overnight.

2.6. Interaction with Toluene. The appropriate aerogel sample was placed in a Horiba solid-state plate sample holder. The surface was smoothed with a spatula, covered with a crystal glass plate, and measured at an angle of 22.5°, with excitation at 380 nm. A drop of toluene was added to the sample well containing the specimen, and the interaction between toluene and the sample was monitored through changes in the fluorescence intensity at specific time intervals: 10 min, 1, 2, and 18 h. However, consistent sample positioning during measurements proved to be challenging, particularly due to the dynamic changes in fluorescence as toluene evaporated. Consequently, certain data sets were omitted due to variability (for **P1C2F** and **P1C3F**), and the results presented here should be considered preliminary. Nonetheless, they offer valuable initial insights into the dynamic interaction of toluene with the dye and aerogel materials. The presented data have been carefully selected for their robustness and their capacity to clearly illustrate the main trends and mechanisms under investigation.

2.7. Adsorption Experiments. A PP aerogel (10 mg) was dipped in 10 mL of toluene aqueous solution (200 mg/L) for 24 h under stirring at room temperature in a sealed glass vial. The amount of toluene adsorbed by the aerogel was obtained using a UV/vis spectrometer (PerkinElmer, Lambda 35); from the calibration curve, the initial and final toluene concentrations in water were determined. The absorbed quantity was

https://doi.org/10.1021/acsomega.4c10168
ACS Omega 2025, 10, 13954−13965

converted to the mass of toluene absorbed (mg)/mass of PP aerogel (g) by using eq 1

$$q_e = \frac{(c_0 - c_e) \times V}{m} \quad (1)$$

where c_0 and c_e are the initial and equilibrium toluene concentrations (mg/L), respectively, V is the volume of the aqueous solution (L), and m is the weight of the aerogel (g). The toluene concentration was taken from the UV absorption peak at 261 nm through a calibration curve.

Blank samples were included in the test runs to account for adsorption due to the experimental material only and, mainly, for the evaporation of toluene during manipulation.

2.8. PP Film Preparation. Powdered samples were dissolved in *p*-xylene/methyl ethyl ketone (3/2, 2.5 mL total) at 120 °C (10 min max), and thereafter, the hot solution was drop-cast onto glass. The samples were left at ambient conditions overnight and then dried under reduced pressure (0.2 mbar, ∼3 h). The flat solid films were characterized by scanning electron microscopy (SEM) (Helios 5 PFIB Cxe DualBeam FIB-SEM; accelerating voltage, 0.5 kV; probe current, 3.1 pA; images in the topographical contrast were acquired using a TLD detector in the BD mode) and contact angle measurements (drop shape analyzer-Krüss-advance, software 1.16 DSA-30, at least 20 measurements per sample).

3. RESULTS AND DISCUSSION

PP-CANs were constructed by the reaction of maleated isotactic PPs (**P1** or **P2**) with capped-end block polyether alcohols **C1**−**C3** in an equimolar ratio (Scheme 1). The

Scheme 1. Reaction Path Leading to the Thermoreversibly Crosslinked Fluorescent PP Networks and Structures of the Crosslinkers

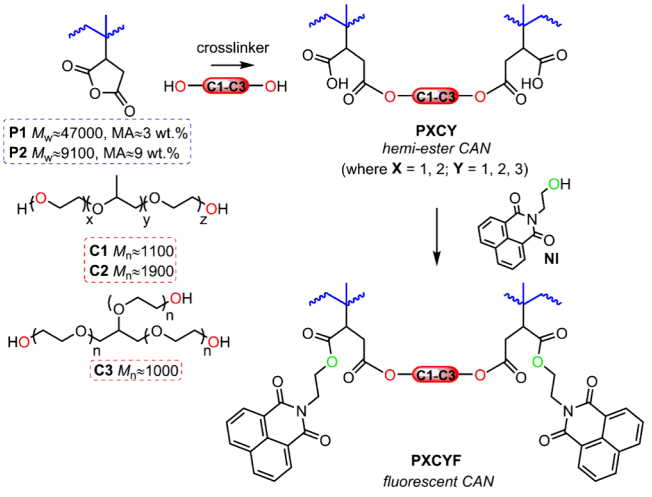

optimal conditions for esterification were achieved using a DMAP-catalyzed mixed anhydride system.[40,41] This catalytic system was also employed for the post polymer modification with the fluorescence **NI** unit (see Experimental Section). The reaction between the maleic and hydroxy groups, leading to a hemiester formation, was monitored by FTIR analyses. For instance, the vibrational bands of the parent polymer **P2** at 1770 and 1712 cm^{-1}, which are assigned to the carbonyl vibrations of maleic anhydride and the carboxylic acid group (formed by hydrolysis under wet storage conditions), respectively, were significantly reduced upon reaction with crosslinker **C2** (Figure 1). A new carbonyl vibration located at

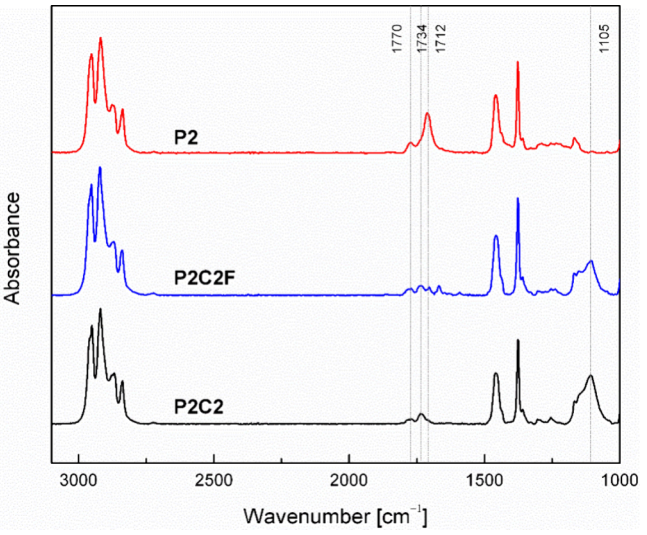

Figure 1. FTIR spectra of the crosslinked polymer **P2** (**P2C2**) and fluorescent-labeled network **P2C2F**.

1734 cm^{-1} appeared, which is assigned to the ester group. Additionally, the intensive vibrational band at 1105 cm^{-1}, assigned to the C−O vibrations of the polyether chain of the crosslinker, was slightly reduced upon the reaction of the polymer network with **NI**, forming **P2C2F**. This reduction may indicate partial de-crosslinking. The other two vibrational bands at 1718 and 1668 cm^{-1} are inherent to the **NI** unit.

The thermoreversibility of the crosslinking was investigated using DSC measurements, as shown in Figure 2. The double

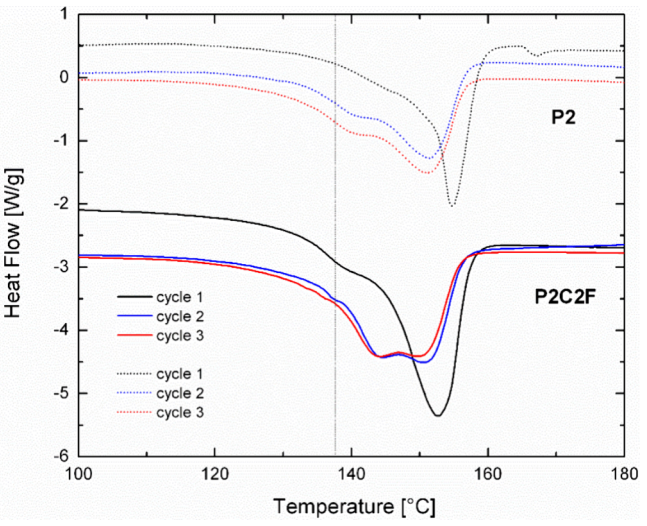

Figure 2. DSC thermograms of heating scans of polymer **P2** (dotted lines) and polymer network **P2C2F** (solid lines) treated with three heating−cooling scans.

endothermic peak at around 140−160 °C is connected with polymer melting and the melting of a small fraction of the random ethylene copolymer of the highly isotactic PP.[42] Evidence of the thermoreversibility is demonstrated by the shoulder peak centered at 138 °C, indicating cleavage of the ester bonds in **P2C2F**. After being subjected to three heating−

https://doi.org/10.1021/acsomega.4c10168
ACS Omega 2025, 10, 13954−13965

cooling cycles, DSC heating scans still present a noticeable peak around the same position. This is a clear indication of the reformation of covalent ester bonds during subsequent cooling, a peak that is notably absent in the parent polymer **P2**. Therefore, it is expected that the material can be reprocessed at elevated temperatures. Moreover, this covalent crosslinking provides a more environmentally friendly alternative for polyolefin crosslinking.

The thermoresponsive behavior was further investigated by variable-temperature IR spectroscopy. As shown in the spectra in the difference mode (initial spectrum at 25 °C subtracted) for the parent polymer **P2** in Figure 3 (top), the intensity of the vibrational band at 1712 cm^{-1}, assigned to the carboxylic acid group, was significantly reduced on increasing the temperature. At the same time, the intensity of vibrational bands around 1770 and 1850 cm^{-1}, assigned to the asymmetric and symmetric carbonyl vibration of the maleic anhydride group, respectively, increased as cyclization to the anhydride between carboxylic groups occurred. Meanwhile, one can transiently observe the appearance of a new vibrational band at 1750 cm^{-1}, originating from carbonyl vibrations associated with carboxylic groups, among which the hydrogen bonding is disrupted by the increased temperature. A similar pattern is observed for the polymer network **P2C2** (Figure 3, middle), and moreover, the intensity of the vibrational band around 1730 cm^{-1} associated with ester groups is reduced by increasing the temperature. These changes are most pronounced when the temperature reaches 140 °C, which corresponds with the observations from DSC (vide supra). After cooling back to 25 °C, no significant changes were observed except the higher content of maleic anhydride groups with respect to the state before the heating procedure, thus providing proof of the thermoreversibility of cross linking. Finally, similar changes were also observed for the polymer network **P2C2F** (Figure 3, bottom), but they are less intense.

The thermally induced phase separation (TIPS) method was used for the preparation of aerogels from the prepared polymer networks. Here, homogeneous solutions were prepared at an elevated temperature. After phase separation, achieved by cooling the polymer solution, the diluent in the wet gels was replaced by acetone. The gels were subsequently dried by using a facile freeze-drying method. The highly porous nanostructural features of interconnected 3D networks are shown in Figure 4. Microscopically, all aerogels exhibit similar morphologies composed of spongy aggregates of spherulites and fibrilates with uniformly interconnected pores. These nanostructural hierarchical features generally fall within the lower tens of nanometers. An increase in the inhomogeneity and size of pores, along with a lower degree of porosity, was observed for the aerogel derived from polymer **P2**. This may be due to the denser packing of polymer chains, an observation consistent with the BET results (vide infra). Additionally, it was shown that the introduction of the **NI** unit into the polymer network did not affect the aerogel morphology, as demonstrated by the comparison with the **P1C1** aerogel (see Figure S13 and Table 1).

Significant differences in morphology and pore structure are evident when compared to the previous literature on PP porous materials. For example, a cellular pore morphology with a pore size of around 9−17 μm was reported for PP membranes prepared by TIPS.[22] Similarly, the PP sponge reported by Wang and Uyama,[25] prepared by the TIPS method, exhibited a macroporous structure with an average

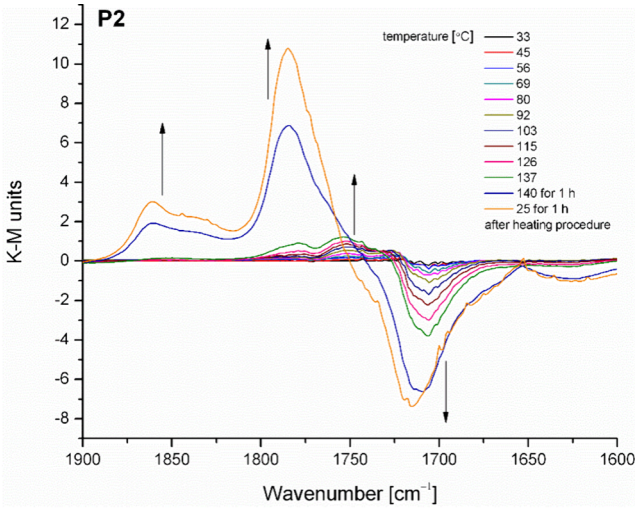

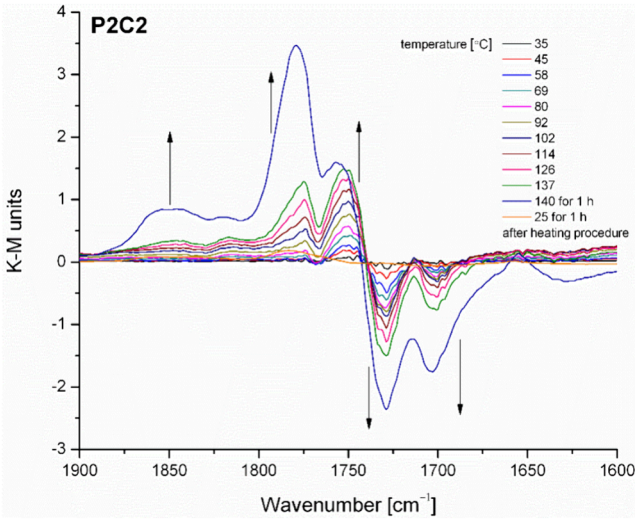

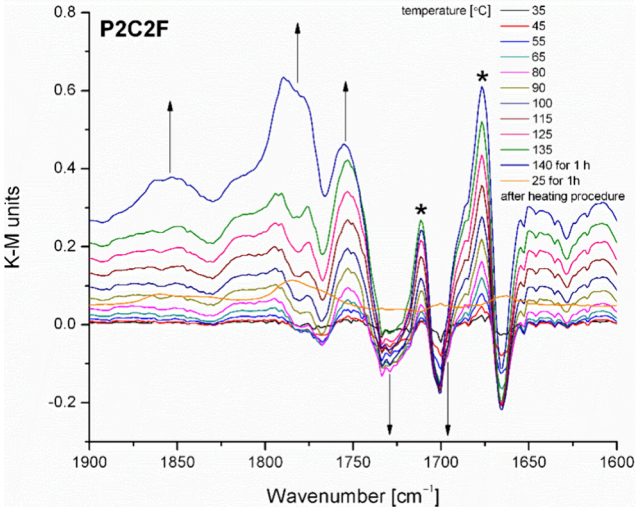

Figure 3. Variable-temperature IR spectra of the parent polymer **P2** (top) and polymer networks **P2C2** (middle) and **P2C2F** (bottom). The spectra are shown in the difference mode (initial spectrum at 25 °C subtracted). * indicates the vibrational band associated with the **NI** unit.

https://doi.org/10.1021/acsomega.4c10168
ACS Omega 2025, 10, 13954−13965

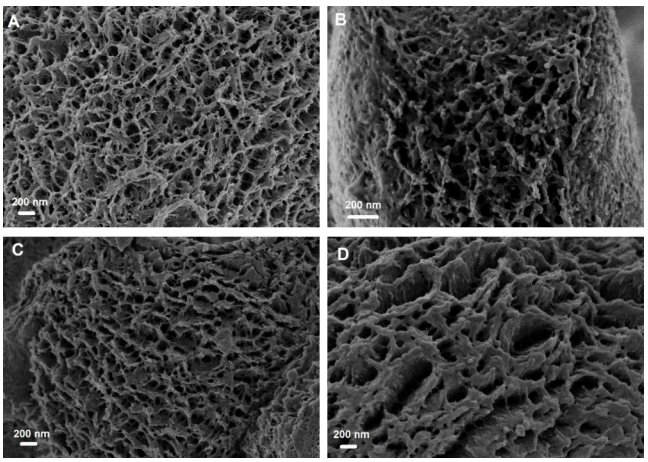

Figure 4. SEM micrographs of the aerogels: (A) **P1C1F**, (B) **P1C2F**, (C) **P1C3F**, and (D) **P2C2F**.

Table 1. Summary of the Specific Surface Area, Pore Volume, and Average Pore Width of Aerogels

aerogel	specific surface area [m^2/g]	pore volume [cm^3/g]	average pore width [nm]
P1C1[a]	191	0.77	10
P1C1F	185	0.74	10
P1C2F	172	0.71	11
P1C3F	172	0.70	10
P2C2F	103	0.33	8

[a]Refer to Figure S13 for graphical data.

pore size of approximately 5 μm. In contrast, the aerogel architectures reported here are similar to those we reported recently using crosslinking without dynamics.[32] This comparison highlights that while other TIPS-prepared PP materials tend to have larger macropores, the dynamic crosslinking approach used in the current study results in a nanostructured aerogel with interconnected 3D networks and smaller pore sizes. This structural characteristic is advantageous for applications requiring a high surface area and porosity, as achieved in our aerogels.

The pore structure of the aerogels was probed by nitrogen absorption and desorption measurements. The nitrogen adsorption−desorption isotherms at 77 K and the pore size distribution profiles are shown in Figure 5. The data on surface area, pore volume, and average pore width are summarized in Table 1. The N_2 absorption isotherms do not reach a well-defined saturation plateau at high relative pressures, indicating a large portion of the macropores. Simultaneously, the shapes of the isotherms suggest that the materials are mesoporous, with average pore widths between 8 and 11 nm and a relatively narrow pore size distribution. The shapes of the hysteresis loops, characterized by parallel branches, suggest the presence of cylindrical pores. The pore volume and average pore width were determined using the desorption branches of isotherms by applying the BJH model.[43] Similar values for specific surface area, pore volume, and average pore width were achieved independent of the crosslinker used with polymer **P1**. However, the specific surface area and pore volume of the aerogel **P2C2F** were significantly lower compared to those of the aerogels made from polymer **P1**. This difference may be due to variations in the structural arrangement, inhomogeneities, and surface defects, corresponding with SEM observations, resulting in significant changes in porosity.

The skeletal framework of the aerogels was further examined using SAXS, which revealed more detailed information about their structures. Representative X-ray scattering profiles are shown in Figure 6. Several models, including the Beaucage unified model, were applied over the entire Q-range, but the fits were of low quality. However, the scattering profiles are characterized by well-separated curvatures, allowing for analysis using the classical Guinier and power-law equations[44,45] with minimum subjectivity. The structural levels consist of power-law regions I and III, which appear linear on the log−log plots in Figure 6, and the Guinier knee regions II and IV, indicative of characteristic length scales. These regions are roughly separated by vertical lines in Figure 6 to facilitate the identification of different structural levels. The Guinier regions indicate the presence of characteristic length scales

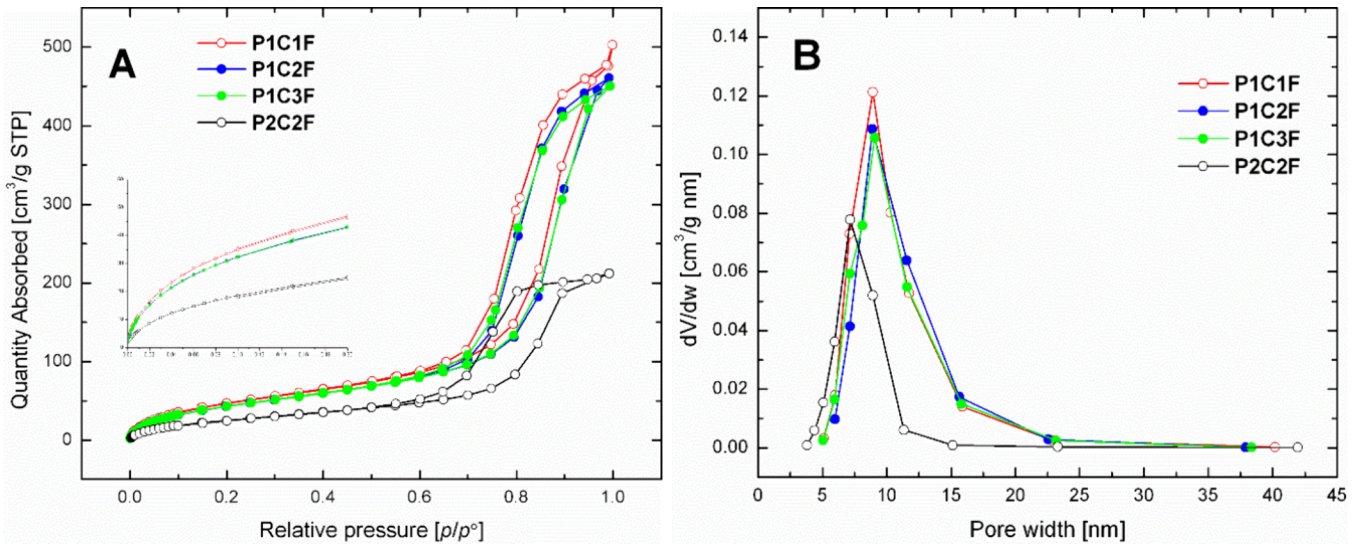

Figure 5. N_2 adsorption−desorption isotherms of aerogels (A) and their pore size distribution profiles (B). To enhance clarity on the porous nature, an isotherm to p/p_0 = 0.2 is included as an inset.

https://doi.org/10.1021/acsomega.4c10168
ACS Omega 2025, 10, 13954−13965

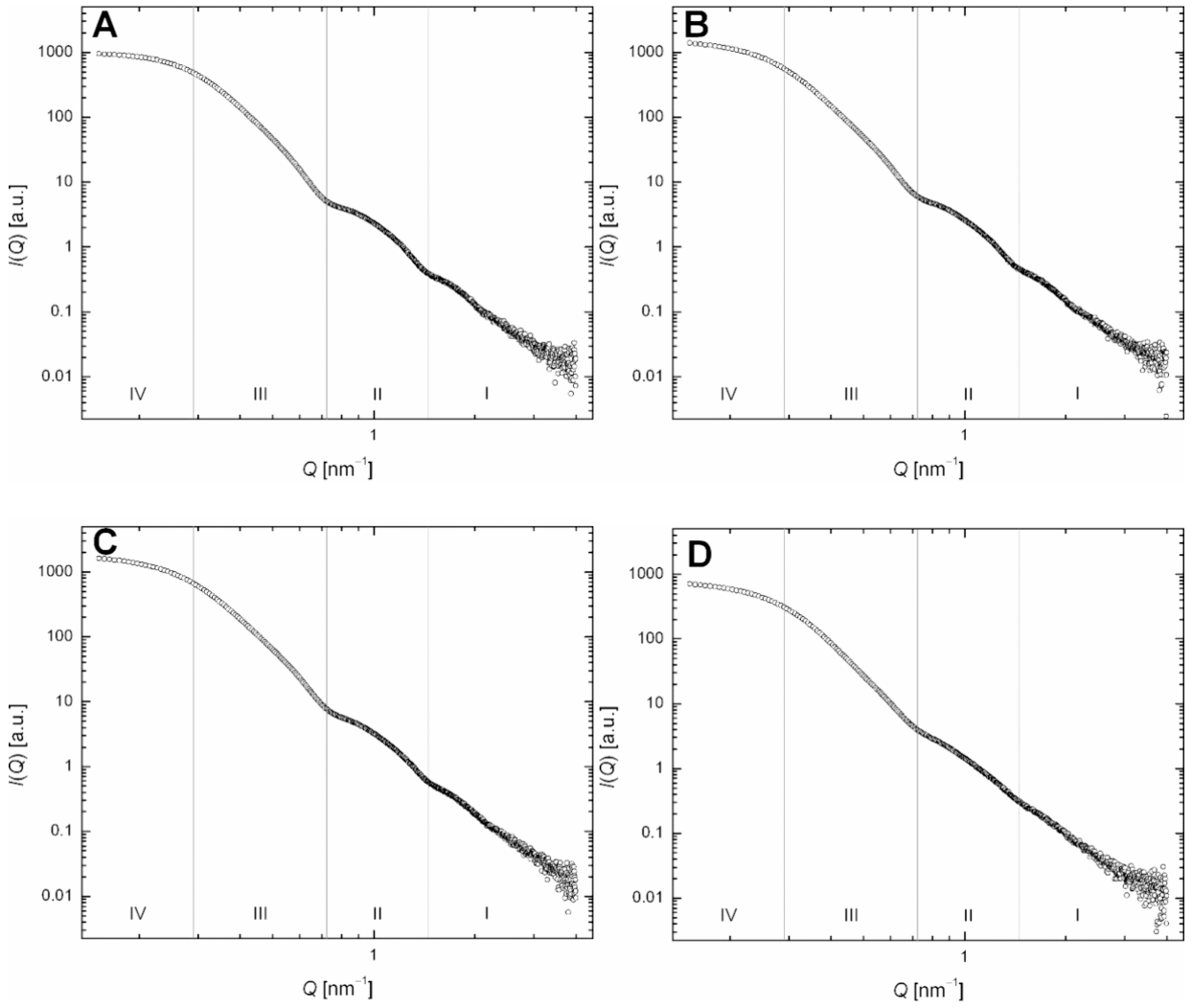

Figure 6. SAXS analyses of aerogels. (A) **P1C1F**, (B) **P1C2F**, (C) **P1C3F**, and (D) **P2C2F** (refer to Table 2 for information on the SAXS data).

associated with the aerogel structures, while the power-law regions provide information about the fractal dimensions and the nature of the scattering entities within the aerogels. This combination of Guinier and power-law analyses helps in understanding the hierarchical organization and the distribution of pores and particles within the aerogels, contributing to the comprehensive characterization of their skeletal frameworks.

Strictly speaking, the Guinier analysis is valid only for highly dilute particle systems. However, it is possible to derive the aggregate size under the assumption of independent scattering.[46] The high-Q Porod-law region (I), with a slight oscillation of intensity at $Q \sim 1.8$ nm^{-1}, is attributed to primary aggregates and provides information about the surface characteristics of the primary aggregates themselves. The slopes of the data in region I yield surface fractal dimensions D_s to be in the range of 2.5−2.8, indicating uneven and rough surfaces (Table 2). The Q-region that roughly corresponds to region II was approximated by the extended Guinier analysis, yielding the radii of gyration R_g (1) of the primary aggregates to be in the narrow range of 2.2−2.3 nm. This suggests that the primary aggregates are composed of closely packed PP segments, with almost no influence from the crosslinker. All samples display similar R_g values, indicating that the primary aggregates in all samples are of comparable size. The slopes of the second, lower-Q power-law region, corresponding to region III, were lower than −4, indicating that the primary aggregates assemble into the secondary aggregates nonfractally. The radii of gyration of the secondary particles R_g (2) were calculated from the second low-Q curvature of the scattering profile (region IV) and ranged from 6.6 to 7.2 nm, indicating a noticeable effect of the crosslinker. The length scale of the secondary aggregates also corresponds to the SEM observations. Furthermore, combining SAXS and SEM results suggest that the lower values of surface characteristics obtained from BET for aerogel **P2C2F** are caused by structural effects at the macroporous level, as the SAXS results on the nanoscale level

Table 2. SAXS Data for Aerogels with Reference to Figure 6

aerogel	D_S[a]	R_g (1) [nm][b]	R_g (2) [nm][c]
P1C1[d]	2.6	2.2	6.7
P1C1F	2.7	2.3	6.6
P1C2F	2.6	2.3	7.2
P1C3F	2.5	2.2	7.1
P2C2F	2.8	2.3	6.9

[a]Surface fractal dimensions of primary aggregates from power-law region I. [b]Radius of gyration of primary aggregates from the Guinier region II. [c]Radius of gyration of secondary aggregates from the Guinier region IV. [d]Refer to Figure S13 for graphical data.

https://doi.org/10.1021/acsomega.4c10168
ACS Omega 2025, 10, 13954−13965

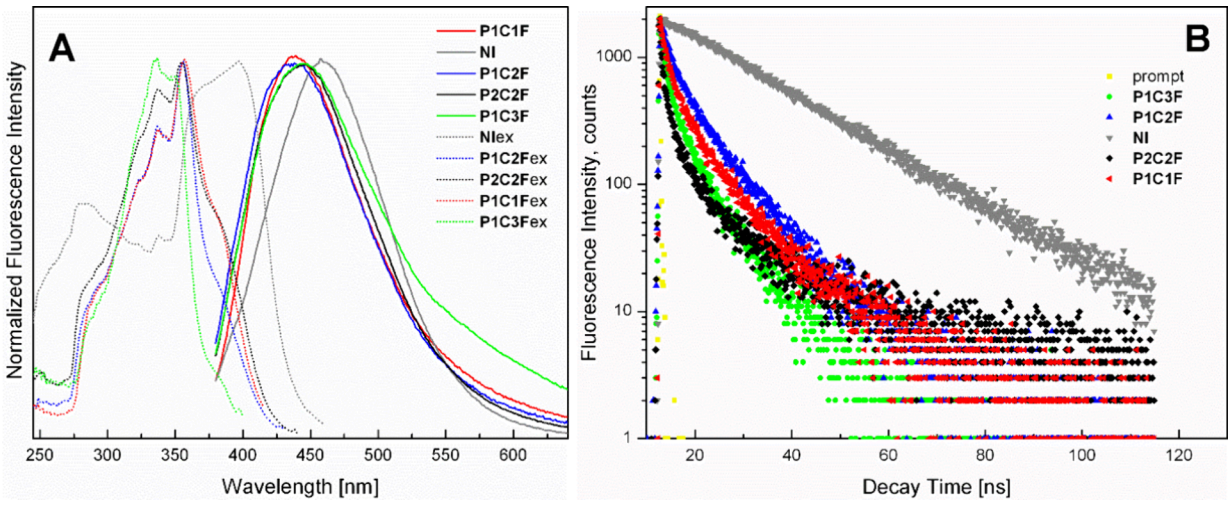

Figure 7. Emission (solid) and excitation (dotted) spectra (A) and natural log of fluorescence decays (B) of **NI** and aerogels; λ_{exc} = 370 nm, the excitation diode in fluorescence decays was held at 372 nm, and the emission wavelength was 450 nm.

provide values similar to those of the other aerogels. This indicates that while nanoscale structures are consistent across different aerogels, macroporous structural differences significantly impact the BET surface area measurements.

In summary, while all samples share some common structural features, distinct differences in their surface roughness and aggregate sizes highlight their unique characteristics. The sizes of the primary aggregates are fairly consistent across all samples, indicating uniformity in their fundamental building blocks. However, the secondary aggregates show more variation, potentially affecting the bulk properties of the aerogels such as their porosity.

The thermal stability of the aerogels was studied by TGA, and the TGA curves are illustrated in Figure S14. The aerogels decompose at 450−460 °C at a sharp rate. The study proved that all of the samples decompose at approximately the same temperature, independent of the parent polymer or crosslinker.

In the emission and excitation spectra presented in Figure 7A, notable differences are observed between the free dye (**NI**) and the dye bound to the polymer. These differences, seen in both emission and excitation spectra, reflect the significant influence of the polymer matrix on the behavior of the dye. The excitation spectrum of free **NI** shows a sharp absorption band around 400 nm. The spectrum is relatively well-defined, with minimal influence from its environment, as expected in a free dye sample. Additionally, the spectrum shows a broad shoulder around 275 nm. This shoulder suggests the presence of higher-energy electronic states that contribute to the absorption behavior of the free dye. The appearance of the broad shoulder seen in the excitation spectrum of the free dye is diminished or truncated in the dye bound to the polymer network, suggesting that the polymer environment restricts access to certain higher-energy states. Shifts in the excitation maxima suggest that the polymer slightly alters the electronic structure of the dye. These shifts indicate that the energy required for excitation is modified, likely due to interactions between the dye and the polymer, such as changes in polarity or specific dye−polymer interactions that stabilize or destabilize certain electronic transitions.

Regarding the emission spectra, the free dye exhibits a sharp and intense emission peak around 460 nm. The emission maxima of the aerogels are significantly blue-shifted compared to the free **NI** unit. This optical response may be attributed to the reduced aggregation and intermolecular charge transfer of **NI** following the incorporation into the polymer network.[47] Importantly, the strong fluorescence of **NI** is preserved within the network architecture, even though only a very low amount of **NI** is incorporated, as determined by the degree of grafting on the PP chain. This demonstrates the effectiveness of the functionalization process in maintaining the optical properties of the NI units within the aerogel structure. The results are summarized in Table S1 and are further supported by the measurement of time-resolved decays.

The decay profiles for all samples in Figure 7B demonstrate both fast and slow components, indicative of multiexponential decay dynamics. The free **NI** luminophore shows a relatively simple monoexponential decay, with a lifetime of approximately 19.6 ns, suggesting a single dominant emissive state, likely free from significant quenching effects or nonradiative decay mechanisms, although at higher wavenumbers, possible formations of the excimers could be observed, indicated by the negative pre-exponential factors in the mathematic fits. However, for the bound luminophore, the polymer network introduces additional pathways for decay, reflected by the appearance of the shorter decay components. Table 3 presents the fitted fluorescence decay time constants, with the relative contributions of individual component to the overall decay. Aerogel **P2C2F**, for instance, exhibits both a fast decay component at around 1.1 ns (44%) and a slower component at 12.7 ns (56%), indicating significant nonradiative deactivation. This could result from energy transfer processes or quenching within the polymer matrix. The polymer environment likely facilitates these interactions, causing a faster decay of excited

Table 3. Fluorescence Decay Time Constants τ_1 and τ_2 (in Nanoseconds) of NI and Aerogels

sample	τ_1 [ns]	τ_2 [ns]
NI	19.6	
P1C1F	10.0 (60%)	1.8 (40%)
P1C2F	8.9 (74%)	1.5 (26%)
P1C3F	9.0 (64%)	1.4 (36%)
P2C2F	12.7 (56%)	1.1 (44%)

https://doi.org/10.1021/acsomega.4c10168
ACS Omega 2025, 10, 13954−13965

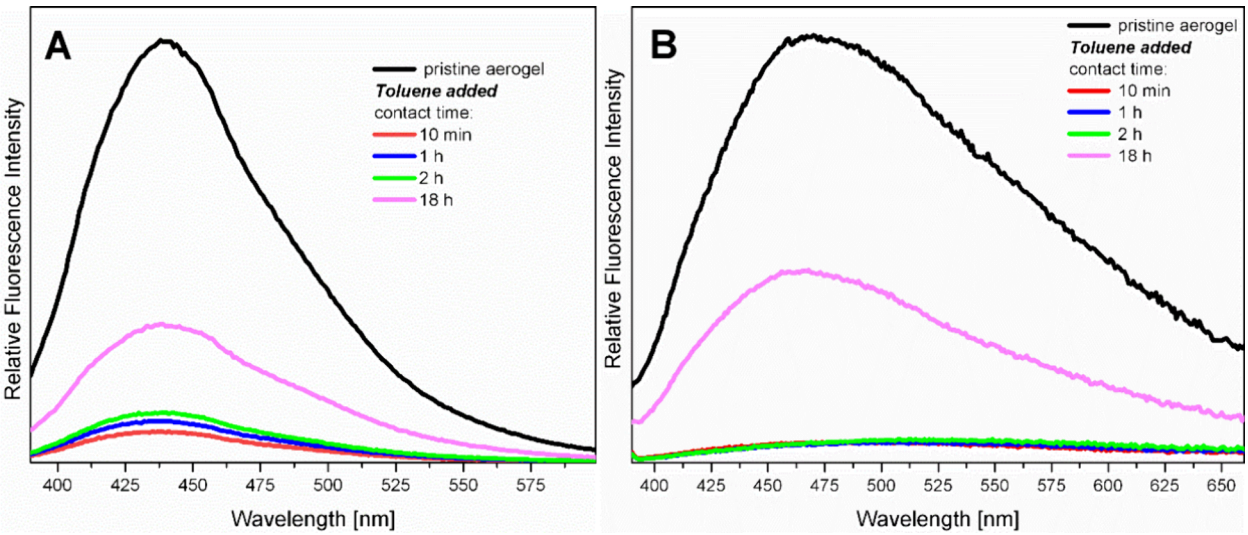

Figure 8. Emission spectra of aerogel **P1C1F** (A) and **P2C2F** (B) before and after the addition of toluene.

states. **P1C1F** shows a biexponential decay (10.0 and 1.8 ns components), further suggesting the involvement of the polymer matrix in mediating the excited-state dynamics. Similarly, **P1C3F** demonstrates a primary decay at 9.00 ns (64%) and a faster component at 1.4 ns (36%), again highlighting the role of the polymer matrix in accelerating nonradiative processes.

The evaluation of the TRES (Figures S15 and S16) did not yield any unexpected results, although the analysis encountered certain challenges due to the solid state, as the granular nature of the polymer made it difficult to ensure uniform positioning of the sample. To account for this, control measurements were repeated with the sample placed in different positions, confirming the consistency of the data despite the variability in the sample distribution. The evaluated curves were mathematically fitted using a Python 3.7 script with a log-normal function. For the pure **NI** dye, the shifts in the emission maxima were marginal as time progressed and did not cause significant broadening or narrowing of the emission peak. The changes in full width at half-maximum (fwhm) were within the detection limits of the method used, indicating minimal structural or environmental perturbations affecting the dye in its free state. Upon binding the **NI** to the polymer matrix, the observed blue shift became less pronounced (Figure S15), and there was a minor but detectable narrowing of the fwhm (Figure S16), particularly for sample **P1C3F**, where this narrowing was most evident. This again demonstrates sensitivity to the polymer matrix, affecting molecular freedom and interactions with the chromophore. In summary, the TRES and decay profiles demonstrate that the polymer matrix has a significant impact on the photophysical behavior of the bound luminophore. The free **NI** dye exhibits relatively simple monoexponential decay and stable emission maxima, while the polymer-bound samples show more complex decay dynamics, including fast and slow decay components, along with broader, blue-shifted emission spectra. These findings highlight the importance of the polymer environment in modulating the excited-state properties of luminophores with potential implications for applications in fluorescence sensing, optoelectronic devices, and other areas where a controlled photophysical behavior is critical.

To shed light on the possible applications, the interactions between aerogels and toluene as a common representative of volatile organic compounds (VOCs) were investigated by fluorescence spectroscopy (see the Experimental Section). Significant fluorescence quenching was observed in all cases within the first 10 min after the addition of toluene. This rapid decrease suggests $\pi-\pi$ interactions between the electron-rich toluene molecules and the electron-deficient **NI**, likely involving intermolecular charge transfer suppressing fluorescence. For the pristine **NI**, the relative luminescence intensity recovered quickly as toluene evaporated (see Figure S17). In aerogel-containing samples, as shown in Figure 8, the evaporation of toluene was notably slower. This delayed evaporation suggests a strong physical interaction, involving van der Waals forces and hydrophobic interactions,[48] between toluene molecules and the porous aerogel matrix. The prolonged quenching indicates a deeper penetration of toluene into the porous structure, leading to extended retention of the toluene within the nanoporous network with extensive sorption sites and spaces for toluene entrapment.

Although the high sorption performance of PP aerogels of lipophilic organic compounds might be expected, as reviewed in the Introduction and demonstrated above, the adsorption from aqueous solutions has not been addressed. This is due to the low surface energy and high hydrophobicity of PP causing strongly limited interfacial molecular transport. However, our preliminary results show a rather surprising efficiency in the adsorption of toluene from aqueous solution. The results of toluene adsorption are presented in Figure S18. The toluene uptakes of aerogels **P1C1F**, **P1C2F**, and **P1C3F** are almost identical, ranging between 12 and 15 mg/g. The toluene uptake from the **P2C2F** aerogel is significantly higher, i.e., 20 mg/g, than that for the aerogels from the P1 polymer. This indicates the possible surface activation of the **P2C2F** aerogel corresponding with the higher density of polar groups on polymer P2 leading to the more efficient interfacial molecular transport between the hydrophilic solution and hydrophobic surface. To support this, the PP coatings obtained by casting onto glass slides from solution were subjected to the water contact angle measurements (see the Experimental Section). The coatings of **P1C2F** and **P2C2F** were homogeneous over the whole area (see Figure S19). On the other hand, the

https://doi.org/10.1021/acsomega.4c10168
ACS Omega 2025, 10, 13954−13965

coatings of **P1C1F** and **P1C3F** suffered from inhomogeneity, and the results from the measurement were omitted due to the significant variability; there were cracks throughout the whole coatings. Nevertheless, the comparison between **P2C2F** surface with a contact angle of 141° ± 5° and **P1C2F** surface with a contact angle of 159° ± 8° clearly demonstrate the transition from a hydrophobic to a superhydrophobic surface and thus a lowering of the surface energy. This is the main factor affecting interfacial molecular transport, which is more efficient in our case for **P2C2F**.

Thorough and complex studies will be separately conducted to discover the potential in adsorption of VOC pollutants from aqueous solutions. Finally, we emphasize the importance of experimental corrections when handling with VOC, because of rapid evaporation when using common laboratory techniques, as was observed in our study, possibly causing significant experimental errors. Hence, it is necessary to include blank samples in the test runs, as in our study, to account mainly for the evaporation of toluene during manipulation. Unfortunately, such a practice is not quite common in the literature.

4. CONCLUSIONS

In summary, a group of highly porous PP-based materials with fluorescent functionality were prepared by exploiting a facile synthetic strategy and low-cost precursors. The implementation of thermoreversible crosslinks offers significant benefits for further material processing and recycling. Combined BET, SEM, and SAXS analyses were employed to elucidate the porous architecture of the aerogels. The aerogels retained the photoluminescent response of the covalently bound fluorescent probe even when incorporated in a low amount. The importance of the polymer environment in modulating the excited-state properties of the luminophore was demonstrated, with potential implications for applications in areas where controlled photophysical behavior is critical. This advantageous feature replaces the conventional use of heavy-metal-based quantum dots in aerogels. The steric hindrance of the PP network restricts the aggregation of fluorophores, leading to shifted emissive features in the solid states. The study also highlights the dynamic interaction between toluene and the neat luminophore and aerogel samples. While fluorescence quenching and recovery were observed for the luminophore, the aerogels demonstrated a pronounced ability to retain toluene, affecting the fluorescence behavior over extended time scales. The results provide an intriguing direction for future research focusing on the molecular mechanisms driving the observed fluorescence with the aim to target the design of functional hydrophobic materials, which could specifically facilitate adsorption or sorption of oil molecules. The built strategy for preparing functional porous PP-based materials is expected to be taken as a potent platform for further exploration and the design of high-performance recyclable materials, particularly for applications such as the sorption or adsorption of various organic molecules in connection with sensing.

■ ASSOCIATED CONTENT

Supporting Information

The Supporting Information is available free of charge at https://pubs.acs.org/doi/10.1021/acsomega.4c10168.

Diagram of the freeze-drying apparatus (Figure S1), IR spectra of PP networks (Figures S2−S4), DSC thermograms (Figures S5−S12), experimental data for the P1C1 aerogel (Figure S13), TGA curves (Figure S14), supporting fluorescence analysis (Figures S15 and S16), emission spectra of the pristine NI before and after addition of toluene (Figure S17), results of toluene adsorption (Figure S18), and characterization of glass coatings (Figure S19) (PDF)

■ AUTHOR INFORMATION

Corresponding Author

Radek Coufal − *Department of Science and Research, Faculty of Health Studies and Department of Advanced Materials, Institute for Nanomaterials, Advanced Technologies and Innovation (CXI), Technical University of Liberec, 461 17 Liberec, Czech Republic;* orcid.org/0000-0002-7386-0824; Email: radek.coufal@tul.cz

Authors

Kinga Adach − *Department of Advanced Materials, Institute for Nanomaterials, Advanced Technologies and Innovation (CXI), Technical University of Liberec, 461 17 Liberec, Czech Republic*

Jiří Zedník − *Department of Physical and Macromolecular Chemistry, Faculty of Science, Charles University, Prague 2 128 43, Czech Republic;* orcid.org/0000-0001-7325-8684

Olga Buchar Klinovská − *Department of Science and Research, Faculty of Health Studies, Technical University of Liberec, 461 17 Liberec, Czech Republic*

Stanislav Petrík − *Department of Advanced Materials, Institute for Nanomaterials, Advanced Technologies and Innovation (CXI), Technical University of Liberec, 461 17 Liberec, Czech Republic*

Mateusz Fijalkowski − *Department of Advanced Materials, Institute for Nanomaterials, Advanced Technologies and Innovation (CXI), Technical University of Liberec, 461 17 Liberec, Czech Republic*

Complete contact information is available at: https://pubs.acs.org/10.1021/acsomega.4c10168

Notes

The authors declare no competing financial interest.

■ ACKNOWLEDGMENTS

We acknowledge CMS-Biocev (Biophysical Techniques, Crystallization, Diffraction, Structural Mass Spectrometry) of CIISB, Instruct-CZ Centre, supported by MEYS CR (LM2023042) and CZ.02.1.01/0.0/0.0/18_046/0015974. We also acknowledge the assistance from prof. Roman Bulánek (University of Pardubice) with measurement and interpretation of variable-temperature IR spectroscopy.

■ REFERENCES

(1) Maleki, H.; Durães, L.; García-González, C. A.; del Gaudio, P.; Prtugal, A.; Mahmoudi, M. Synthesis and biomedical applications of aerogels: Possibilities and challenges. *Adv. Colloid Interface Sci.* **2016**, *236*, 1−27.

(2) Fijalkowski, M.; Coufal, R.; Ali, A.; Adach, K.; Petrík, S.; Bu, H.; Karl, Ch. W. Flexible Hybrid and Single-Component Aerogels: Synthesis, Characterization, and Applications. *Langmuir* **2023**, *39*, 16760−16775.

(3) Moreno-Castilla, C.; Maldonado-Hódar, F. J. Carbon aerogels for catalysis applications: An overview. *Carbon* **2005**, *43*, 455−465.

(4) Wang, R.; Li, G.; Dong, Y.; Chi, Y.; Chen, G. Carbon Quantum Dot-Functionalized Aerogels for NO_2 Gas Sensing. *Anal. Chem.* **2013**, *85*, 8065−8069.
(5) Yang, J.; Zhang, E.; Li, X.; Zhang, Y.; Qu, J.; Yu, Z.-Z. Cellulose/graphene aerogel supported phase change composites with high thermal conductivity and good shape stability for thermal energy storage. *Carbon* **2016**, *98*, 50−57.
(6) Ferreira-Gonçalves, T.; Constantin, C.; Neagu, M.; Pinto Reis, C.; Sabri, F.; Simón-Vázquez, R. Safety and efficacy assessment of aerogels for biomedical applications. *Biomed. Pharmocother.* **2021**, *144*, No. 112356.
(7) Kistler, S. S. Coherent Expanded Aerogels and Jellies. *Nature* **1931**, *127*, 741.
(8) Pekala, R. W. Organic aerogels from the polycondensation of resorcinol with formaldehyde. *J. Mater. Sci.* **1989**, *24*, 3221−3227.
(9) Shea, K. J.; Loy, D. A.; Polysilsesquioxanes, Bridged Molecular-Engineered Hybrid Organic-Inorganic Materials. *Chem. Mater.* **2001**, *13*, 3306−3319.
(10) Cashman, J. L.; Nquyen, B. N.; Dosa, B.; Meador, M. A. B. Flexible Polyimide Aerogels Derived from the Use of a Neopentyl Spacer in the Backbone. *ACS Appl. Polym. Mater.* **2020**, *2*, 2179−2189.
(11) Meador, M. A. B.; Wright, S.; Sandberg, A.; Nguyen, B. N.; Van Keuls, F. W.; Mueller, C. H.; Rodríguez-Solís, R.; Miranda, F. A. Low Dielectric Polyimide Aerogels As Substrates for Lightweight Patch Antennas. *ACS Appl. Mater. Interfaces* **2012**, *4*, 6346−6353.
(12) Meador, M. A. B.; McMillon, E.; Sandberg, A.; Barrios, E.; Wilmoth, N. G.; Mueller, C. H.; Miranda, F. A. Dielectric and Other Properties of Polyimide Aerogels Containing Fluorinated Blocks. *ACS Appl. Mater. Interfaces* **2014**, *6*, 6062−6068.
(13) Guo, H.; Meador, M. A. B.; McCorkle, L.; Quade, D. J.; Guo, J.; Hamilton, B.; Cakmak, M. Tailoring Properties of Cross-Linked Polyimide Aerogels for Better Moisture Resistance, Flexibility, and Strength, *ACS Appl. Mater, Interfaces* **2012**, *4*, 5422−5429.
(14) Pantoja, M.; Boynton, N.; Cavicchi, K. A.; Dosa, B.; Cashman, J. L.; Meador, M. A. B. Increased Flexibility in Polyimide Aerogels Using Aliphatic Spacers in the Polymer Backbone. *ACS Appl. Mater. Interfaces* **2019**, *11*, 9425−9437.
(15) Leventis, N.; Sotiriou-Leventis, Ch.; Mohite, D. P.; Larimore, Z. J.; Mang, J. T.; Churu, G.; Lu, H. Polyimide Aerogels by Ring-Opening Metathesis Polymerization (ROMP). *Chem. Mater.* **2011**, *23*, 2250−2261.
(16) Bang, A.; Buback, C.; Sotiriou-Leventis, Ch.; Leventis, N. Flexible Aerogels from Hyperbranched Polyurethanes: Probing the Role of Molecular Rigidity with Poly(Urethane Acrylates) Versus Poly(Urethane Norbornenes). *Chem. Mater.* **2014**, *26*, 6979−6983.
(17) Shinko, A.; Jana, S. C.; Meador, M. A. Crosslinked polyurea-*co*-polyurethane aerogels with hierarchical structures and low stiffness. *J. Non-Cryst. Solids* **2018**, *487*, 19−27.
(18) Chidambareswarapattar, Ch.; McCarver, P. M.; Luo, H.; Lu, H.; Sotiriou-Leventis, Ch.; Leventis, N. Fractal Multiscale Nanoporous Polyurethanes: Flexible to Extremely Rigid Aerogels from Multifunctional Small Molecules. *Chem. Mater.* **2013**, *25*, 3205−3224.
(19) Donthula, S.; Mandal, Ch.; Leventis, T.; Schisler, J.; Saeed, A. M.; Sotiriou-Leventis, Ch.; Leventis, N. Shape Memory Superelastic Poly(isocyanurate-urethane) Aerogels (PIR-PUR) for Deployable Panels and Biomimetic Applications. *Chem. Mater.* **2017**, *29*, 4461−4477.
(20) Erbil, H. Y.; Demirel, A. L.; Avci, Y.; Mert, O. Transformation of a Simple Plastic into a Superhydrophobic Surface. *Science* **2003**, *299*, 1377−1380.
(21) Lin, Y. K.; Chen, G.; Yang, J.; Wang, X. L. Formation of isotactic polyprolylene membranes with bicontinuous structure and good strength via thermally induced phase separation method. *Desalination* **2009**, *236*, 8−15.
(22) Othman, N.; Harruddin, N.; Idris, A.; Ooi, Z.-Y.; Fatiha, N.; Norimie, R.; Sulaiman, R. Fabrication of polypropylene membrane via thermally induced phase separation as a support matrix of tridodecylamine supported liquid membrane for red 3BS dye removal. *Desalin. Water Treat.* **2015**, *57*, 12287.
(23) Lang, X. H.; Zhu, T. Y.; Zou, L.; Prakashan, K.; Zhang, Z. X. Fabrication and characterization of polypropylene aerogel coated hybrid materials for oil-water separation applications. *Prog. Org. Coat.* **2019**, *137*, No. 105370.
(24) Hong, H.; Pan, Y.; Sun, H.; Zhu, Z.; Ma, Ch.; Wang, B.; Liang, W.; Yang, B.; Li, A. Superwetting polypropylene aerogel supported form-stable phase change materials with extremely high organics loading and enhanced thermal conductivity. *Sol. Energy Mater. Sol. Cells* **2018**, *174*, 307−313.
(25) Wang, G.; Uyama, H. Facile synthesis of flexible microporous polypropylene sponges for separation of oil and water. *Sci. Rep.* **2016**, *6*, 21265−21270.
(26) Saleem, J.; Moghal, Z. K. B.; McKay, G. Designing super-fast trimodal sponges using recycled polypropylene for organics cleanup. *Sci. Rep.* **2023**, *13*, 14163−14174.
(27) Choi, H.; Parale, V. G.; Lee, K.-Y.; Nah, H.-Y.; Driss, Z.; Driss, D.; Bouabidi, A.; Euchy, S.; Park, H.-H. Polypropylene/Silica Aerogel Composite Incorporating a Conformal Coating of Methyltrimethoxysilane-Based Aerogel. *J. Nanosci. Nanotehnol.* **2019**, *19*, 1376−1381.
(28) Yoda, S.; Takeshita, S.; Ono, T.; Tada, R.; Ota, H. Development of a New Silica Aerogel-Polypropylene Foam Composite as a Highly Flexible Thermal Insulation Material. *Front. Mater.* **2021**, *8*, No. 674846.
(29) Abdolmaleki, H.; Jafari, S. H.; Golriz, M.; Haghgoo, M. Polypropylene aerogel-based composites with paraffin and MWCNTs as phase change materials. *Polym. Eng. Sci.* **2024**, *64*, 3188−3202.
(30) Létoffé, A.; García-Rodríguez, S. M.; Hoppe, S.; Canilho, N.; Godard, O.; Pasc, A.; Royaud, I.; Ponçot, M. Switching from brittle to ductile isotactic polypropylene-*g*-maleic anhydride by crosslinking with capped-end polyether diamine. *Polymer* **2019**, *164*, 67−78.
(31) Létoffé, A.; Hoppe, S.; Lainé, R.; Canilho, N.; Pasc, A.; Rouxel, D.; Riobóo, R. J. J.; Hupont, S.; Royaud, I.; Ponçot, M. Resilience improvement of an isotactic polypropylene-g-maleic anhydride by crosslinking using polyether triamine agents. *Polymer* **2019**, *179*, No. 121655.
(32) Coufal, R.; Fijalkowski, M.; Adach, K.; Bu, H.; Karl, C. W.; Mikysková, E.; Petrík, S. Preparation and Investigation of High Surface Area Aerogels from Crosslinked Polypropylenes. *Polymers* **2024**, *16*, 1382.
(33) Gao, Y.; Niu, H. Polypropylene-based transesterification covalent adaptable networks with internal catalysis. *Polym. Chem.* **2024**, *15*, 884−895.
(34) Benissen, W.; Winne, J. M.; Du Prez, F. E. Vitrimeers: permanent organic networks with glass-like fluidity. *Chem. Sci.* **2016**, *7*, 30−38.
(35) Elling, B. R.; Dichtel, W. R. Reprocessable Cross-Linked Polymer Networks: Are Associative Exchange Mechanisms Desirable? *ACS Cent. Sci.* **2020**, *6*, 1488−1496.
(36) Dong, H.-Q.; Wei, T.-B.; Ma, X. Q.; Yang, Q.-Y.; Zhang, Y.-F.; Sun, Y.-J.; Shi, B.-B.; Yao, H.; Zhang, Y.-M.; Lin, Q. 1, 8-Naphthalimide-Based Fluorescent Chemosensors: recent advances and perspectives. *J. Mater. Chem. C* **2020**, *8*, 13501−13529.
(37) Wang, H.; Shao, Z.; Bacher, M.; Liebner, F.; Rosenau, T. Fluorescent cellulose aerogels containing covalently immobilized $(ZnS)_x(CuInS_2)_{1-x}$/ZnS (core/shell) quantum dots. *Cellulose* **2013**, *20*, 3007−3024.
(38) Wei, S.; Zhang, Z.; Xu, Y.; Dang, D.; Zeng, R. Covalent Installation of Fluorophores into Polyethylene: Synthesis, Characterization, and Applications. *Macromolecules* **2024**, *57*, 3595−3603.
(39) Kohlbrecher, J.; Breßler, I. Updated in SASfit for fitting analytical expressions and numerical models to small-angle scattering patterns. *J. Appl. Crystallogr.* **2022**, *55*, 1677−1688.
(40) Sakakura, A.; Kawajiri, K.; Ohkubo, T.; Kosugi, Y.; Ishihara, K. Widely Useful DMAP-Catalyzed Esterification under Auxiliary Base- and Solvent-Free Conditions. *J. Am. Chem. Soc.* **2007**, *129*, 14775−14779.

https://doi.org/10.1021/acsomega.4c10168
ACS Omega 2025, 10, 13954−13965

(41) Shiina, I.; Kubora, M.; Oshiumi, H.; Hashizume, M. An Effective Use of Benzoic Anhydride and Its Derivatives for the Synthesis of Carboxylic Esters and Lactones: A Powerful and Convenient Mixed Anhydride Method Promoted by Basic Catalysts. *J. Org. Chem.* **2004**, *69*, 1822−1830.
(42) Gartner, C.; Suárez, M.; López, B. L. Grafting of maleic anhydride on polypropylene and its effect on blending with poly(ethylene terephthalate). *Polym. Eng. Sci.* **2008**, *48*, 1910−1916.
(43) Kruk, M.; Jaroniec, M. Gas Absorption Characterization of Ordered Organic-Inorganic Nanocomposite Materials. *Chem. Mater.* **2001**, *13*, 3169−3183.
(44) Tamon, H.; Ishizaka, H. SAXS Study on Gelation Process in Preparation of Resorcinol-Formaldehyde Aerogel. *J. Colloid Interface Sci.* **1998**, *206*, 577−582.
(45) Carsughi, F. Simplified Polydispersion Analysis of Small-Angle Scattering Data. *Appl. Sci.* **2022**, *12*, 10677.
(46) Emmerling, A.; Fricke, J. Small angle scattering and the structure of aerogels. *J. Non-Cryst. Solids* **1992**, *145*, 113−120.
(47) Al-Kaysi, R. O.; Ahn, T. S.; Müller, A. M.; Bardeen, C. J. The photophysical properties of chrmophores at high (100 mM and above) concentrations in polymers and as neat solids. *Phys. Chem. Chem. Phys.* **2006**, *8*, 3453−3459.
(48) Dutta, S.; Sinelshchikova, A.; Andreo, J.; Wuttke, S. Nanoscience and nanotechnology for water remediation: an earnest hope toward sustainability. *Nanoscale Horiz.* **2024**, *9*, 885−899.

https://doi.org/10.1021/acsomega.4c10168
ACS Omega 2025, 10, 13954−13965